Polypeptide Composite Particle-Assisted Organization of π-Conjugated Polymers into Highly Crystalline "Coffee Stains"

Cornelia Rosu,[*,†,‡,#] Ping-Hsun Chu,[‡] Christopher J. Tassone,[§] Katherine Park,[∥] Paul L. Balding,[⊥] Jung Ok Park,[†,▽] Mohan Srinivasarao,[†,‡,#] and Elsa Reichmanis[*,†,‡,⊥,#]

[†]School of Materials Science and Engineering, [‡]School of Chemical and Biomolecular Engineering, [⊥]School of Chemistry and Biochemistry, [#]Georgia Tech Polymer Network, and [▽]Center for Science and Technology of Advanced Materials and Interfaces, Georgia Institute of Technology, Atlanta, Georgia 30332, United States

[§]Stanford Synchrotron Radiation Lightsource, Stanford Linear Accelerator Center, Stanford, California 94025, United States

[∥]Molecular Vista, Inc., 6840 Via Del Oro, Suite 110, San Jose, California 95119, United States

ABSTRACT: We demonstrate that homopolypeptides covalently tethered to anisotropically shaped silica particles induce crystalline ordering of representative semiconducting polymers. Films drop-cast from chloroform dispersions of poly(γ-stearyl-L-glutamate) (PSLG) composite particles and poly(3-hexythiophene) (P3HT) led to highly ordered crystalline structures of P3HT. Hydrophobic–hydrophobic interactions between the alkyl side chains of P3HT and PSLG were the main driving force for P3HT chain ordering into the crystalline assemblies. It was found that the orientation of rigid P3HT fibrils on the substrate adopted the directionality of the evaporating front. Regardless of the PSLG-coated particle dimensions used, the drop-cast films displayed patterns that were shaped by the coffee ring and Marangoni effects. PSLG-coated particles of high axial ratio (4.2) were more efficient in enhancing the electronic performance of P3HT than low axial ratio (2.6) homologues. Devices fabricated from the ordered assemblies displayed improved charge-carrier transport performance when compared to devices fabricated from P3HT alone. These results suggest that PSLG can favorably mediate the organization of semiconducting polymers.

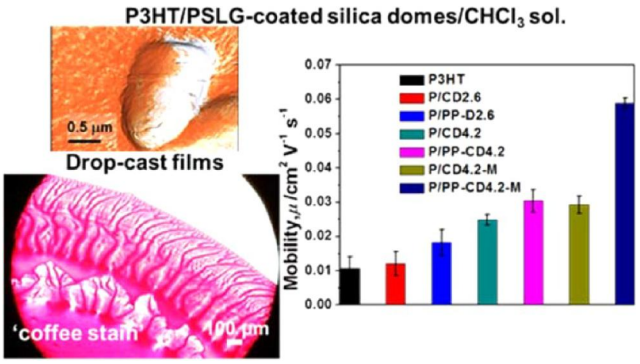

KEYWORDS: *polypeptide-assisted self-assembly, Marangoni flow, coffee ring effect, semiconducting polymers, electronic materials, OFET devices*

1. INTRODUCTION

Conjugated polymers are a class of functional materials whose performance is known to depend upon polymer structure, orientation, and self-assembly.[1] The organization and alignment of semiconducting polymers into highly ordered structures over macroscopic length scales is a longstanding goal;[2−7] the extent of ordering significantly influences electronic performance of the active material.[8] Self-assembly occurs by $\pi-\pi$ stacking of polymer chains that ideally propagates over large distances[9] and facilitates intra- and interchain charge transport.[10] Chain self-assembly generates crystalline domains surrounded by amorphous regions, leading to the formation of grain boundaries and defects.[11,12] These defects limit charge-carrier transport and thus electronic performance.[6,13,14] A particularly important feature associated with improved charge transport in polymer semiconductors is enhanced planarization of the backbone that ensures effective packing of the polymer chains into well-organized assemblies.[3] This characteristic depends on the chosen processing protocol.[4,5,15−25]

Owing to powerful self-assembly capacities, natural and synthetic biopolymers are appealing tools to assist organization of functional polymers. In support of this idea, Cerato ulmin, a fungal protein,[26,27] facilitated the formation of poly(3-hexythiophene) (P3HT) condensed phases of remarkably high crystallinity upon encapsulation by a self-assembled biofilm.[28] Efforts toward designing bioinspired semiconductors with interesting self-assembly behaviors also involved synthetic peptides and oligothiophene conjugates.[29,30] Polypeptides are compounds that lack the complex amino acid sequence and structure of natural proteins, a feature making them appealing for large-scale use. Recently, self-assembled bundles of rodlike poly(γ-benzyl-L-glutamate) (PBLG) in toluene assisted the organization of P3HT into three-dimensional (3D) networks.[31] The resulting gels showed reversible thermal and photophysical responses.

The synthetic polypeptide poly(γ-stearyl-L-glutamate) (PSLG) is one of the less-explored polypeptides for its ability to self-assemble and induce ordering.[32] Like PBLG, PSLG has a single amino acid repeat unit and both belong to the so-called synthetic homopolypeptide class. PSLG forms lyotropic cholesteric liquid crystals in various organic solvents, especially ones that promote an α-helical conformation.[33] This ordering of PSLG in solution was exploited to organize symmetric and asymmetric polypeptide composite particles into ordered structures.[34,35] The identical chemical nature between the covalently bound particle shell and the matrix led to their compatibility. The hierarchical assemblies showed remarkable stability, owing to hydrophobic−hydrophobic interactions between the PSLG matrix and the particle shell through their stearyl side chains. From these examples, it is expected that similar interactions can be harnessed to increase the performance of functional polymers bearing alkyl groups.

Here, the homopolypeptide PSLG[32] covalently tethered to anisotropically shaped silica particles was used to demonstrate the ability of PSLG to interact with and organize functional materials such as conjugated polymers into ordered, active constructs. These particles are appealing because they act as vehicles carrying a high load of polypeptide. Interactions between the tethered PSLG and the representative π-conjugated polymer P3HT facilitated P3HT alignment and organization. Drop-cast films of P3HT blended with PSLG-tethered particles exhibited highly crystalline order, as evidenced by grazing-incidence wide-angle X-ray scattering (GIWAXS) and polarized micro-Raman spectroscopy. The ability of PSLG to assist in P3HT organization was also reflected in semiconducting performance tested with an organic field-effect transistor (OFET) architecture. The use of polypeptide composite particles to organize semiconducting polymers into ordered structures demonstrates the feasibility of using biopolymers to induce organization of difficult-to-crystallize functional materials.

2. EXPERIMENTAL SECTION

2.1. Materials. Poly(3-hexylthiophene) [P3HT; M_w = 90 000 Da, polydispersity index (PDI) > 2, and regioregularity (RR) = 96%] was purchased from Rieke Metal Inc. Anhydrous chloroform, $CHCl_3$, was obtained from Sigma−Aldrich. The preparation of anisotropic pristine and PSLG-coated silica with and without a magnetic nougat followed literature procedures.[35] Two axial ratios (L/D, length/diameter) were used: 2.6 (low) and 4.2 (high).

2.2. Sample Preparation. A control sample of P3HT in dry $CHCl_3$ (0.5% w/w) was prepared in an 8 mL scintillation vial by heating to 60 °C under magnetic stirring for 20 min until the polymer dissolved and the solution turned to a clear orange color. The dispersions were produced by adding aliquots of particles dispersed in chloroform to the 0.5 wt % P3HT/$CHCl_3$ solutions. Excess chloroform was evaporated under a stream of nitrogen to bring dispersions to the listed concentrations. Table S1 summarizes the specific amounts of dispersion components and their concentrations. All concentrations were calculated from weight.

2.3. Methods. *2.3.1. UV−Visible Spectrometry.* Solid-state UV−vis spectra were recorded on an Agilent 850 UV−vis spectrometer. Thin films were prepared by drop-casting and by spin-casting (WS-650MZ-23NPP, Laurell) the P3HT−particle suspensions onto precleaned glass slides. Before film casting, the glass slides were rinsed sequentially with acetone, methanol, and 2-propanol and the surface was then dried with a nitrogen stream. Afterward they were kept for 30 min in an UV−ozone cleaner (Novascan PSD-UV) to remove contaminants.

2.3.2. Polarized Micro-Raman Spectroscopy. Dry films obtained by drop-casting the dispersions onto glass substrates followed by solvent evaporation were investigated with a micro-Raman spectrometer (Raman Rxn) from Kaiser Optical Systems Inc. The instrument has a 785 nm laser with a resolution of 4 cm^{-1} in backscattering and an integrated polarized light optical microscope equipped with a rotating stage. The instrument is equipped with a Leica DM2500 P polarizing microscope. For all experiments, a 50× objective was used; the laser power was 40 mW and the exposure time was 16 s. The optimum signal-to-noise ratio necessary for reliable peak fitting was achieved with five exposures and five accumulations. Spectra were collected at different angles (0°−180°) of the substrate position with respect to polarizer upon rotating the microscope stage in increments of 10°. The Holograms TM software was used to fit peaks corresponding to the P3HT C=C stretching vibrations to a Lorentzian function.

2.3.3. Polarized Optical Microscopy. A Leica DM 4500P light-emitting diode (LED) microscope equipped with a Canon DS126271 camera (Canon Inc.) was used to analyze the film samples deposited onto glass substrates. The polarizer and analyzer were crossed at 90°. The sample stage was rotated at 45° and 90° to inspect the anisotropic character of the film. Bright-field images were also recorded for comparison.

2.3.4. Confocal and Structured Illumination Microscopy. Confocal and structured illumination images were recorded with an Elyra PS 1 system that can operate in structured illumination mode. Drop-cast samples on the glass substrates were irradiated with the 488 nm (200 mW) laser line.

2.3.5. Atomic Force Microscopy. An Icon Dimension (Bruker) scanning probe microscope operating in tapping mode with a silicon tip (RTESP, Bruker) was used to analyze the surface morphology of the drop-cast semiconducting films.

2.3.6. Photoinduced Force Microscopy. An atomic force microscope (AFM, model VistaScope) from Molecular Vista was used for photoinduced force microscopic (PiFM) measurements. The microscope was operated in tapping mode under ambient conditions. The sample was scanned with a gold-coated cantilever (PPP-NCHAu) from Nanosensors. The force constant was 30 $N \cdot m^{-1}$. The tunable IR excitation source used for the PiFM measurements was a LaserTune from Block Engineering, with ~1 mW of laser power at the sample. AFM topographic images were taken concurrently with PiFM images, while the IR source was tuned to either 1450 cm^{-1} [for thiophene ring characteristic signals (C=C)] or 1660 cm^{-1} (for PSLG amide I signal). PiFM spectra were recorded on the substrate, on and off particle surface from 1350 to 1700 cm^{-1}, with an exposure time of 100 ms/wavenumber.

2.3.7. Organic Field-Effect Transistor Fabrication and Characterization. Bottom-gate, bottom-contact OFET device substrates were assembled in a clean room. First, a 300-nm-thick SiO_2 dielectric layer was grown on a highly doped silicon substrate that served as the gate electrode. Photolithography-based liftoff process and E-beam evaporation (Denton Explorer) techniques were used to deposit 50 nm Au contacts with 3 nm Cr as the adhesion layer. The OFET devices were introduced into a UV−ozone chamber (Novascan PSD-UV) for 15 min to remove any residual photoresist and organic contaminants. This step was performed right before drop-casting of the P3HT-based solution and dispersions (~50 μL). OFET devices holding the P3HT films were dried in vacuo overnight at 50 °C. Device testing was performed in a glovebox under inert atmosphere (nitrogen) with an Agilent 4155C semiconductor parameter analyzer. The field-effect hole mobility was recorded in the saturation regime of transistor operation (V_d = −80 V).

2.3.8. Grazing-Incidence Wide-Angle X-ray Scattering. GIWAXS data were collected at beamline 11-3 at the Stanford Synchrotron Radiation Lightsource. The incident X-ray photon energy was 12.7 keV. Scattered X-rays were collected on a Mar345 image plate detector. For data presented here, the sample incident angle was 0.12°, and the sample-to-detector distance was 400 mm. The beam center position and sample-to-detector distance were calibrated by use of a lanthanum hexaboride standard. Exposure times were in the 90−120 s range.

Scheme 1. Illustration of Drop-Cast Film Preparation[a]

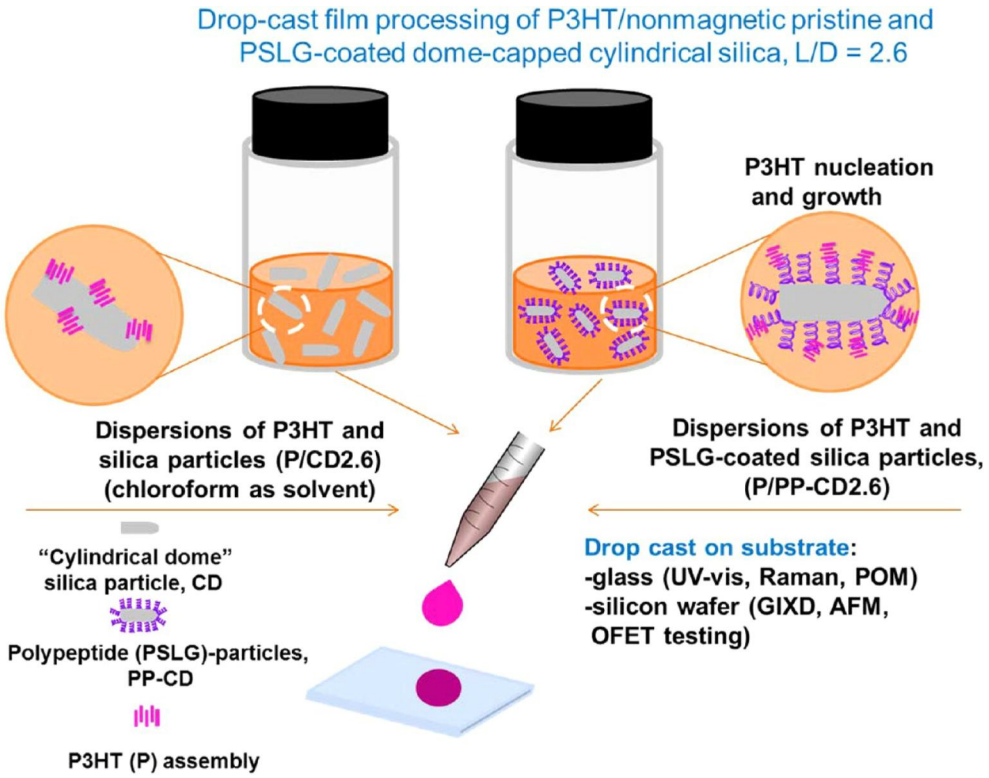

[a]Processed from chloroform dispersions of P3HT containing low axial ratio (L/D = 2.6) particles P/CD2.6 (control), and P/PP-CD2.6. Not drawn to scale.

3. RESULTS AND DISCUSSION

3.1. Processing of Drop-Cast Films. To investigate the polypeptide-assisted organization of polymer semiconductors, silica particles decorated with a dense layer of covalently bound PSLG chains were selected because they provide a convenient means to study PSLG-conjugated polymer interactions.[35] Two axial ratios (L/D) of composite particles (2.6 and 4.2) and identical PSLG loading (10%) were evaluated. For convenient removal from dispersions, magnetic nougats were incorporated into the higher axial ratio particles. Control samples comprising silica particles without the PSLG shell were also examined. Scheme 1 illustrates the sequence of steps associated with the fabrication of drop-cast films containing 2.6 L/D particle dispersions (see Scheme S1 for 4.2 L/D particles). Briefly, designated quantities of PSLG-coated particle dispersions and P3HT in chloroform, as listed in Table S1, were added to scintillation vials and heated at 60 °C to effect P3HT dissolution. After the dispersions turned to clear orange (due to absorption of P3HT), they were allowed to cool to ambient temperature, and ~50 μL from each vial was deposited by drop-casting onto glass and silicon substrates. Abbreviations for the particle-containing dispersions are P/CD2.6, P/PP-CD2.6, P/CD4.2, P/PP-CD4.2, P/CD4.2-M, and P/PP-CD4.2-M, where P/ indicates P3HT, PP represents the polypeptide (PSLG), and M means the particles were magnetically removed before drop-casting. P/PP-CD2.6 and its controls (P3HT and P/CD2.6) were used first to investigate whether PSLG shell has the ability to enhance the organization of P3HT chains (by UV−vis and polarized micro-Raman spectroscopy). Next, the effect of the two L/D PSLG particles on P3HT ordering and electronic performance will be compared.

3.2. PSLG−P3HT Hydrophobic−Hydrophobic Interactions. Photoinduced force microscopy (PiFM) performed on P3HT−particle films fabricated via drop-casting revealed the ability of PSLG to interact with P3HT. The spectra presented in Figure 1 were collected on and off (outside) the particle surface.

Figure 1A presents the superimposed 3D topographic and PiFM spectral images obtained from the P/PP-CD2.6 film surface. The laser source was tuned to the wavelength of the PSLG amide I signal, which occurs at ~1650 cm^{-1}. The strong PiFM signal (orange coloration, Figure 1A) associated with the presence of the excited species confirms the presence of PSLG at the particle surface: the vibration at 1655 cm^{-1} is associated with amide I and reflects its α-helical secondary conformation (Figure 1B).[34,35] Upon tuning the laser to the thiophene ring C=C band (~1450 cm^{-1}; Figure 1C), P3HT was observed at the same location as PSLG (Figure 1B, black trace). The semiconducting polymer was also observed on the silicon substrate (red trace). The appearance of control samples fabricated from P3HT and non-PSLG-bearing particle dispersions was distinctly different. As presented in Figure 1D,E, while P3HT spread uniformly across the substrate, the conjugated polymer was clearly absent on the particle surface. PiFM data suggest that PSLG and P3HT interact in such a way that P3HT appears to anchor to the particle surface. Conceivably, hydrophobic−hydrophobic interactions between the alkyl substituents, C6 (P3HT) and C18 (PSLG), facilitate nucleation of P3HT into ordered structures at the particle surface.

3.3. Photophysical and Anisotropic Optical Behavior. UV−vis analysis, performed on thinner and more uniformly

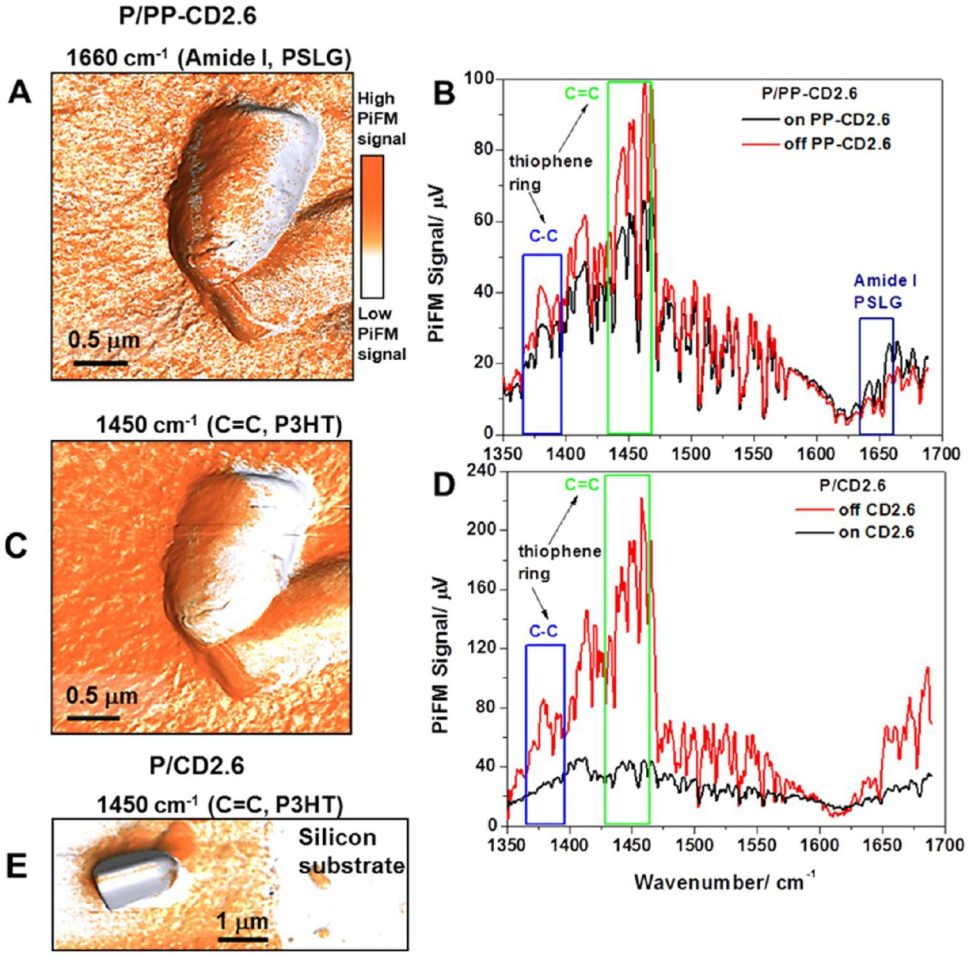

Figure 1. Typical PiFM data. (A, C) Superimposed PiFM spectral and 3D topographic images of P/PP-CD2.6 taken with the laser source tuned for (A) α-helix amide I signal (~1660 cm^{-1}) and (C) thiophene ring C=C signal (1450 cm^{-1}). (B, D) PiFM signal vs wavenumbers recorded on and off (B) P/PP-CD2.6 and (D) P/CD2.6 particle surfaces. (E) Overlay of PiFM and 3D topographic images of P/CD2.6, with laser tuned for P3HT C=C signal (1450 cm^{-1}).

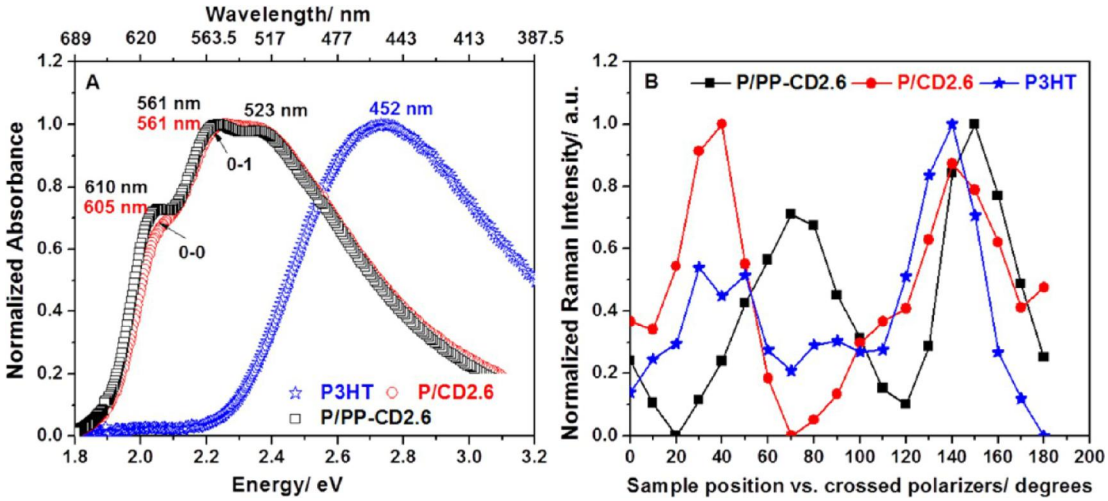

Figure 2. (A) Normalized UV–vis absorption traces and (B) normalized Raman intensities, recorded as a function of sample position vs crossed polarizers, for P3HT (blue), P/CD2.6 (red), and P/PP-CD2.6 (black).

coated films prepared via spin-coating, demonstrated that interactions between the PSLG particles and P3HT chains enhanced semiconductor chain alignment via backbone planarization. Figure 2A shows comparative P3HT spectra with and without particle loading. Pristine P3HT exhibited the anticipated amorphous absorption band at 452 nm (blue trace).

In the presence of CD2.6 versus PP-CD2.6 particles, the conjugated polymer displayed distinctly different results than P3HT alone. The first peak recorded at low energy, 2.03 eV

(610 nm) for P/PP-CD2.6, was slightly red-shifted (5 nm) and more intense than the corresponding band of P/CD2.6 at 2.04 eV (605 nm). A similar trend was visible for the second band: 2.61 eV (561 nm) for P/PP-CD2.6, which represented a red shift of 7.5 nm versus its non-PSLG-bearing counterpart, 2.24 eV (553.5 nm). A third absorbance was observed at 2.37 eV (523 nm) for both particle-containing samples. The lower energy spectral features represent the characteristic (0−0) and (0−1) transitions and suggest enhanced planarization of the P3HT backbone with subsequent self-assembly leading to ordered aggregates.

In order to differentiate the extent of conjugation in the P/PP-CD2.6-processed film versus its control, P/CD2.6, the analysis of Spano and co-workers[36] was applied to evaluate the free exciton bandwidth, W, from the low-energy spectral bands associated with ordered structures [0−0 (intramolecular) and 0−1 (intermolecular) coupling; see Supporting Information].[37] As summarized in Table 1, significant differences in W values were observed for the two films: 53 meV for P/PP-CD2.6 versus 256 meV for P/CD2.6.

Table 1. A_{0-0}/A_{0-1} Ratios and Free Exciton Bandwidth Values[a]

sample	A_{0-0}/A_{0-1}	W (meV)
P/CD2.6	0.33	260
P/PP-CD2.6	0.55	53

[a]Calculated from the model of Spano and co-workers.[36]

The smaller W value associated with sample P/PP-CD2.6 reflects an increase in the conjugation length of the individual polymer chains and also suggests the presence of a higher degree of well-ordered versus disordered structures. Further support for the presence of increased ordering in P/PP-CD2.6 comes from examination of A_{0-0}/A_{0-1} ratios for P3HT in the presence or absence of PSLG. These ratios are 0.55 and 0.33 for P/PP-CD2.6 and P/CD2.6, respectively, which confirms that intrachain coupling (0−0) became more pronounced than interchain coupling (0−1) in films processed from PSLG particle dispersions.[3,38] The UV−vis spectroscopic analysis coupled with PiFM data demonstrates that PSLG is able to interact with and induce organization of the conjugated polymer semiconductor.

Polarized micro-Raman spectroscopy confirmed the alignment of P3HT chains into ordered structures, leading to optical anisotropy.[39] The angle-dependent profile of the thiophene ring intensities associated with C=C and C−C stretching band vibrations displayed in Figure 2B indicates enhanced anisotropy. The position of the C=C and C−C Raman bands implied that, in the presence of PSLG, the polythiophene backbone became more planar. In P/PP-CD2.6, the respective C=C and C−C vibrations were detected at 1445 and 1377 cm^{-1}, identical to P/CD2.6 but at lower frequencies than pristine P3HT (1446 and 1380 cm^{-1}).

The birefringent nature of all studied samples was also evidenced through polarized optical microscopy (POM) (Figure 3). The drop-cast films exhibited two distinct regions: a featureless zone in the center of the drop that was surrounded by a patterned "outer skirt", as seen in bright-field images (Figure 3A,C,E and Figures S1 and S2). At the droplet edge, a transparent ringlike deposit formed upon solvent evaporation (Figure 3E), and three different undulating patterns (fingering, marked as I, II, and III in Figure 3F) appeared to start from the outer ring and traverse the drop's edge-to-center area. Viewed between crossed polarizers (Figure 3B,D,F), the films were bright, suggesting the presence of ordered P3HT domains. Rotation of the sample stage with respect to the polarizer enabled visualization of other details: fingering and alternating rings crossing the fingers were significantly brighter than the body of the drop. No fingering was observed in drop-cast films of PSLG and CP particles alone (Figure S3).

Investigation at high magnification revealed additional interesting features of the films (Figure 4). Upon rotation of P/PP-CD2.6 at 45° with respect to crossed polarizers (Figure 4B), a sharp and smooth isotropic linear pattern divided the bright fingers (II), a feature that was not observed when the sample was set at 0° (Figure 4A). At 0°, the undulating fingers in the P/PP-CD4.2-M film consisted of two parts, a bright region and a faded one (Figure 4C). Upon rotation at 45° (Figure 4D), the bright part seen at 0° became isotropic while the faded area exhibited brightness and seemed divided, in a manner similar to that seen in P/PP-CD2.6 (Figure 4B). The

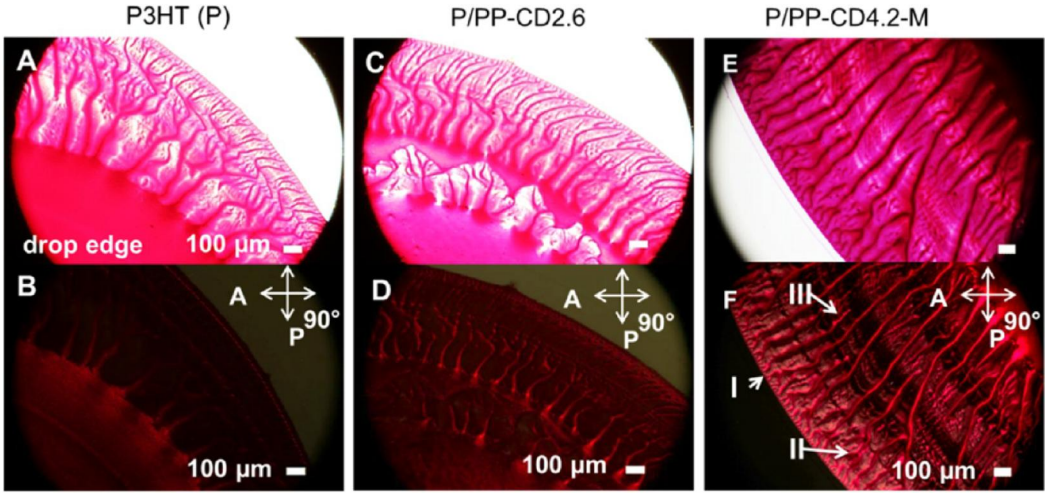

Figure 3. Bright-field and polarized optical micrographs of drop-cast films processed from dispersions of (A, B) P3HT (P); (C, D) low axial ratio particles, P/PP-CD2.6; and (E, F) high axial ratio particles after magnetic removal, P/PP-CD4.2-M. I, II, and III represent the three different undulating periodic patterns observed at the edge of the film.

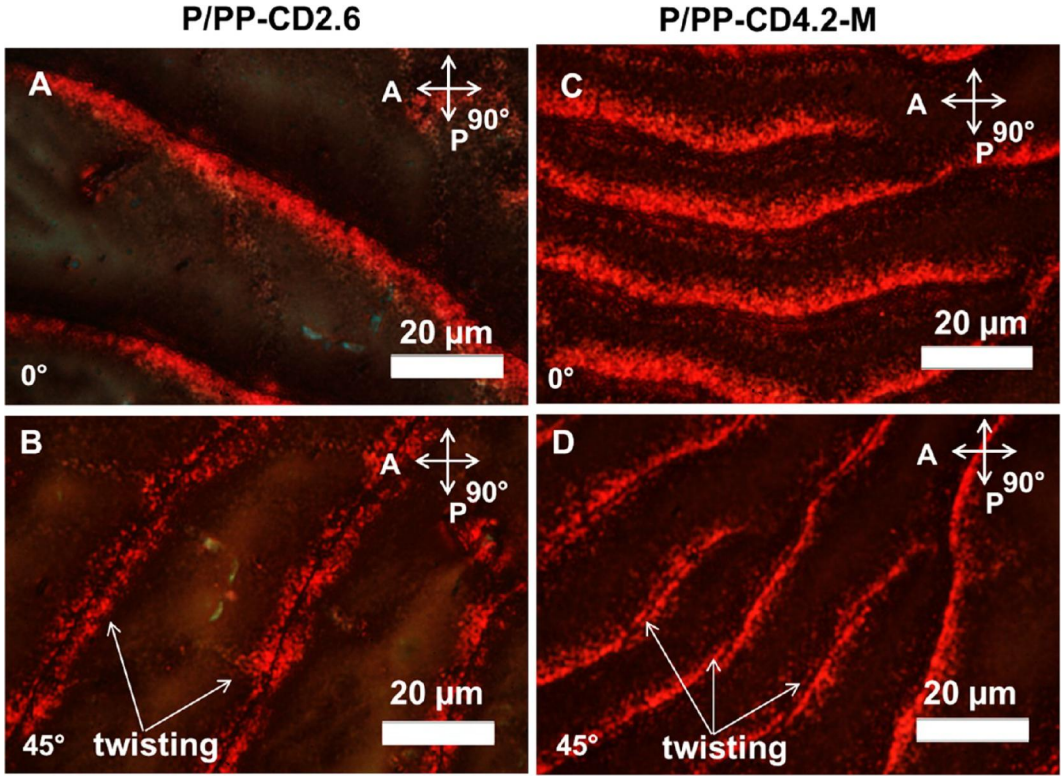

Figure 4. High-magnification POM images of (A, B) P/PP-CD2.6 and (C, D) P/PP-CD4.2-M showing the undulating pattern periodicity and twisting.

bright appeared twisted along the undulating fingers (white arrows, Figure 4B,D). This feature was not observed in control samples (Figure S4). Although the twisting origin requires further in-depth investigation, its occurrence points to intense interactions between P3HT chains and PSLG-coated particles that generate long-range ordering of semiconductor assemblies. A plausible explanation relates to combined drying effects and polymer interactions; they may cause cleavage or breakage of a small amount of PSLG chains from the CP particle surface. These optically active rods may have a similar effect on P3HT assemblies as chiral dopants have on nematic liquid crystal phases.[40,41] The presence of cleaved or broken PSLG chains in the drop-cast film is also suggested by the PiFM data: slight orange coloration, representing PSLG amide I signal, was detected outside the P/PP-CD2.6 particle surface (Figure 1A). Another feature of the patterns denoted as I, II, and III in Figure 3F was their periodicity. The values extracted from the optical images are listed in Table 2. No apparent correlation was observed between the samples containing low and high axial ratio PSLG-coated particles, as well as the particle-free films (withdrawn by magnet). The behavior of these films under polarized light is reminiscent of materials such as cholesteric liquid crystals that present long-range order and periodic patterns.[35,42] The POM, polarized micro-Raman spectroscopy, and UV−vis results suggest that, when processed from PSLG-coated particles, P3HT underwent more extensive ordering than either the PSLG-free silica controls or P3HT alone.

Table 2. Periodicity of Patterns I, II, and III Observed at the Drop-Cast Film Edge

	periodicity (μm)		
sample	pattern I	pattern II	pattern III
P3HT	21.5 ± 2	54.5 ± 16	162.0 ± 35
P/CD2.6	23.0 ± 5	45.0 ± 10	98.0 ± 20
P/PP-CD2.6	17.0 ± 3	27.0 ± 4	82.5 ± 11
P/CD4.2	21.0 ± 4	61.0 ± 20	111.0 ± 20
P/PP-CD4.2	17.0 ± 3	81.5 ± 17	142.0 ± 40
P/CD4.2-M	34.5 ± 9	80.0 ± 16	146.0 ± 34
P/PP-CD4.2-M	20.0 ± 5	48.0 ± 11	162.0 ± 45

3.4. Morphology of Drop-Cast Films. The microstructure of P3HT crystalline structures was further examined by atomic force microscopy (AFM). Figure 5 shows that drop-cast films consist of fibrils, presumably formed as a result of self-assembly through polymer chain $\pi-\pi$ stacking. Pristine P3HT films (Figure 5A) presented less ordered fibers on the substrate when compared to P/PP-CD2.6 (Figure 5B) and P/PP-CD4.2-M (Figure 5C). In all samples, P3HT fibers seem well-defined across the viewing area. Their orientation on the substrate suggests they followed the direction of the evaporating front (white arrows). P3HT fibers were more ordered in the edge to near-center area when compared to the center of the dried drop (Figure 5B). Because the formation of P3HT fibrils accelerates during the drop-cast technique as a result of solvent evaporation, it was not clear whether self-assembled fibers exist in solution prior to film formation. Spin-casting, a technique that leads to rapid solvent evaporation, provided additional insight into the film formation process. The AFM images are shown in Figure S5. Pristine P3HT films appeared pattern-free. Similarly, the P/CD2.6 film surface morphology exhibited no identifiable fiber features. On the other hand, P/PP-CD2.6 films comprised clear fibrils spread across the silicon substrate.

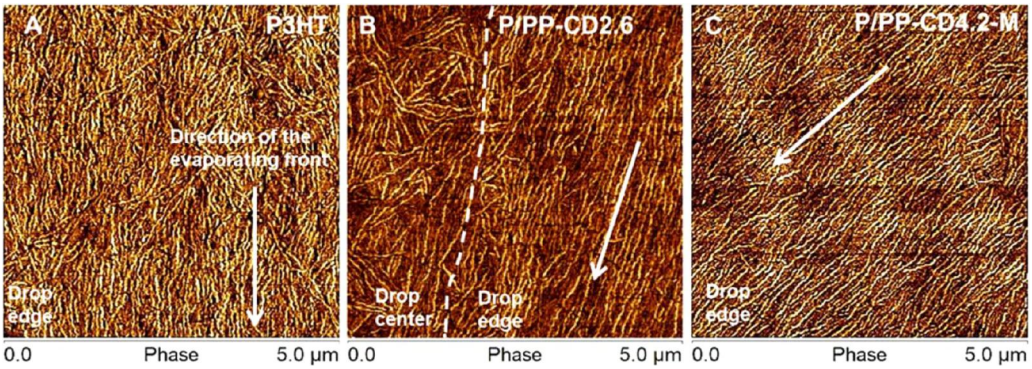

Figure 5. AFM phase images of (A) P3HT, (B) P/PP-CD2.6, and (C) P/PP-CD4.2-M. White arrows represent the direction of the evaporating front. The white dotted line represents the border between the edge and center of the drop-cast film.

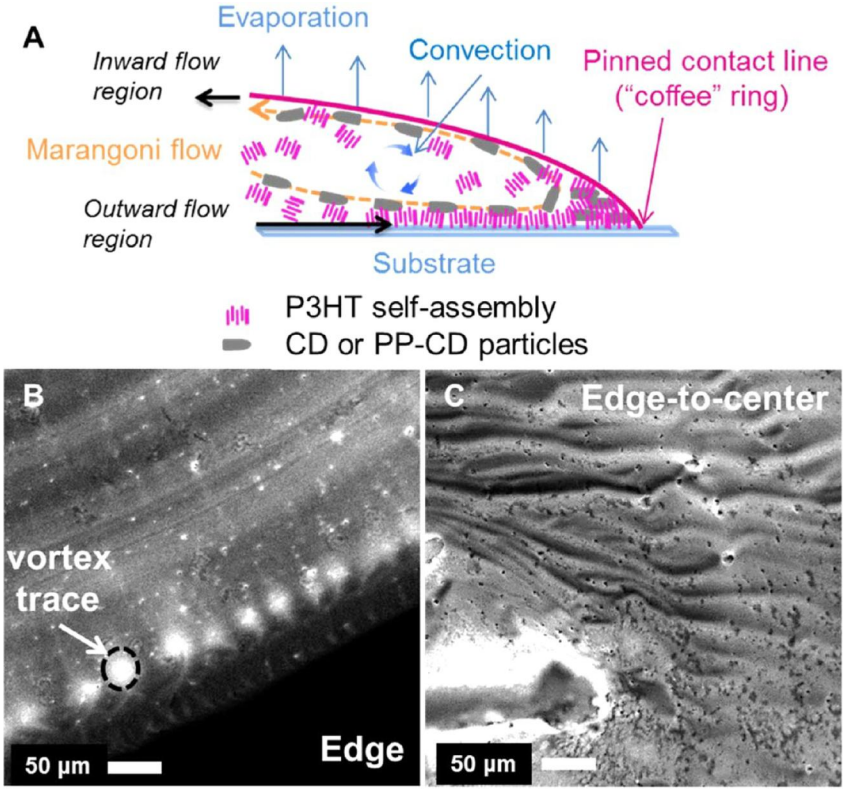

Figure 6. (A) Schematic illustration of coffee ring and Marangoni effects. (B, C) Structured illumination microscopic images of P/PP-CD2.6 recorded (B) at the film's edge and (C) near the center. The white arrow points to apparent vortex traces caused by Marangoni eddy.

Marks of undulating patterns accompanying the P3HT fibrils are reminiscent of the wavy appearance seen in POM (Figure S6). Fibril width varied from the edge to the center, where they appeared to be thicker. AFM analysis coupled to PiFM further suggests that the presence of PSLG on the anisotropic particle surface facilitated P3HT self-assembly into elongated structures (fibrils).

3.5. Coffee Ring and Marangoni Effects. From a mechanistic perspective, the observed undulating patterns in POM and AFM most likely occurred as a result of phenomena associated with droplet drying. The observed film morphologies suggest cooperative and competitive interactions between the coffee ring and Marangoni effects,[43−46] as illustrated in Figure 6A. It is conceivable that these effects synergistically helped to increase the interactions between PSLG and P3HT, leading to highly aligned structures according to the direction of the evaporation front. Solvent evaporation induces an outward capillary flow from the center to the edge and, typically, the particulates form the coffee ring.[47] In the present drop-cast films, the large anisotropic silica particles were not visible within the exterior deposit, indicating that perhaps only impurities and P3HT aggregates were pinned at the film edge. P3HT fluorescence characteristics allowed investigation of drop-cast films with structured illumination microscopy. Whereas fluorescence was too weak in the exterior ring due to insufficient P3HT deposition, a series of regularly spaced linear patterns traversed the near-edge zone, beginning at the outermost ring (Figure 6B). They split into X shapes and merge into round, intensely fluorescent features. Dim, straight lines emanate from these circular zones and become thicker; they ripple across the proximity of the center area, as shown in Figure 6C. Particles appear to follow these undulations in large

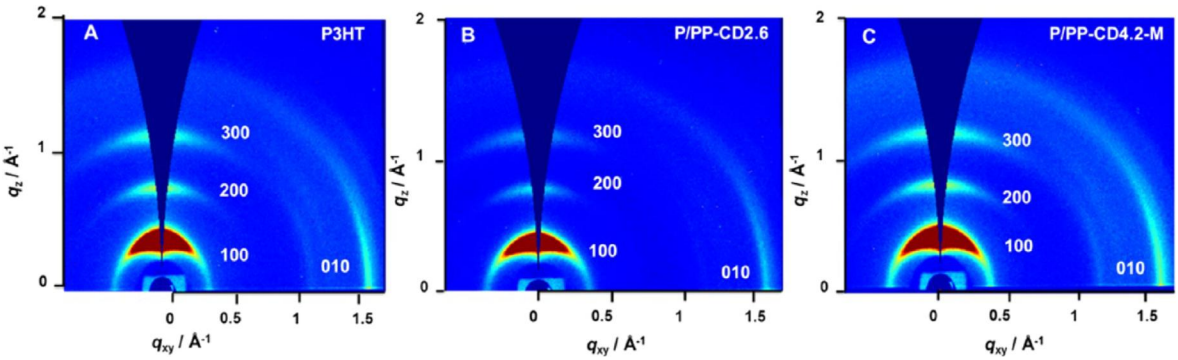

Figure 7. GIWAXS comparative two-dimensional (2D) spectra of films fabricated from (A) P3HT; (B) low axial ratio particles, P/PP-CD2.6; and (C) high axial ratio particles after magnetic removal of particles, P/PP-CD4.2-M.

Table 3. d_{100} and d_{010} Spacing and Associated Scattering Vector Magnitude q Values, Full Width at Half-Maximum, and Crystal Size

sample	q (Å^{-1})	d_{100} (Å)	q (Å^{-1})	d_{010} (Å)	fwhm (deg)	τ (nm)
P3HT	0.390	16.10 ± 0.02	1.640	3.83 ± 0.003	0.070	75 ± 2
P/CD2.6	0.367	17.11 ± 0.01	1.660	3.78 ± 0.004	0.065	81 ± 1
P/PP-CD2.6	0.367	17.11 ± 0.01	1.670	3.76 ± 0.002	0.056	94 ± 4
P/CD4.2	0.390	16.10 ± 0.03	1.650	3.80 ± 0.005	0.075	70 ± 2
P/PP-CD4.2	0.387	16.36 ± 0.02	1.650	3.80 ± 0.001	0.069	76 ± 3
P/CD4.2-M	0.380	16.50 ± 0.03	1.630	3.85 ± 0.002	0.073	71 ± 2
P/PP-CD4.2-M	0.390	16.10 ± 0.01	1.640	3.67 ± 0.002	0.067	78 ± 1

numbers (Figure 6C) when compared to the near-edge region (Figure 6B). The center zone was populated by uniform deposits of particles and P3HT aggregates (Figure S7).

The presence of the X-shaped, circular, and undulating patterns, as well as particle deposits in the droplet center, suggested continuous surface-tension-induced Marangoni flows. Thus, the outward flow that formed the coffee ring was not strong enough to propagate over long distances and was overwhelmed by the inward convective flow at the liquid–air interface (Figure 6A). The evaporating solvent cooled the system and induced temperature and surface tension gradients along the liquid–air interface. Under these conditions, and as suggested by the linear and X-shaped patterns visible in Figure 6B, the outward capillary flow brought particles and P3HT aggregates to the drop edge, but they were repelled and drawn away by the inward flow. The radial flow (vortex) or Marangoni eddy is reflected in the circular, highly fluorescent patterns near the edge (Figure 6B, white arrow).[48]The brightness that accompanies the patterns, regardless of shape, is most probably associated with P3HT molecular alignment enhanced by the Marangoni flow. It is likely that the orientation of P3HT molecule transition dipole moments favorably disposes them to absorb or re-emit light more brightly in these regions. With time, mass transfer from the center toward the edge of the drop increased, but particulates were rejected in large numbers and redeposited uniformly across the drying drop area as a film. The distribution is expected to depend on particle size; larger particles (CD, PP-CD, P3HT aggregates) would be carried further toward the center.[49]

Another characteristic of the film morphology is the presence of multiple tree-ring-like structures in the near-edge area (Figure 6B). During evaporation, the inward convective flow causes rapid depinning and repinning of the three-phase contact line.[50] The newly formed contact lines stabilize themselves by self-pinning. The process takes place several times until only the Marangoni flows dominate the solute deposition. The center of the film has nearly uniform deposits of both P3HT aggregates and CD/PP-CD particles, as seen in Figures S2 and S7. When the dispersion's native P3HT fibrils move with the outward coffee ring and inward Marangoni flows, they also interact with each other. The directed flow can favor fibrils merging into long structures essential to generate crystalline films. It is also possible that the regular structure (fingering) seen across these films formed after edge depinning. Clear separation between the coffee ring and Marangoni effects requires in-depth investigations that are beyond the scope of this report.

3.6. Polypeptide-Assisted P3HT Organization into Ordered Crystalline Structures. Incorporation of PSLG particles into P3HT solutions resulted in birefringent films with improved optoelectronic properties, suggesting enhanced polymer chain ordering. Grazing-incidence wide-angle X-ray scattering (GIWAXS) was used to study the crystalline nature of the drop-cast films.

Figure 7A presents the typical diffraction pattern for a pristine P3HT film. The in-plane (100) and higher order (200 and 300) reflections indicate a perpendicular orientation of the hexyl side chains relative to the substrate, where the π-conjugation axis is preferentially oriented parallel. This disposition of P3HT assemblies relative to substrate is well-known as edge-on. The in-plane (010) peak corresponding to thiophene ring $\pi-\pi$ stacking in pristine P3HT was centered at a d spacing of 3.83 Å ($d = 2\pi q^{-1}$), as shown in Table 3.

The (010) reflection recorded for P3HT in the presence of low axial ratio P/PP-CD2.6 particles was at 3.76 Å (Figure 7B), and that of the P/CD2.6 control was at 3.78 Å (see Figure S8D). In the presence of the higher axial ratio magnetic particles, the d spacing was centered at 3.80 Å in both P/PP-CD4.2 and P/CD4.2 samples (see Figure S8A,B). After the particles were magnetically removed, the 010 reflection was at

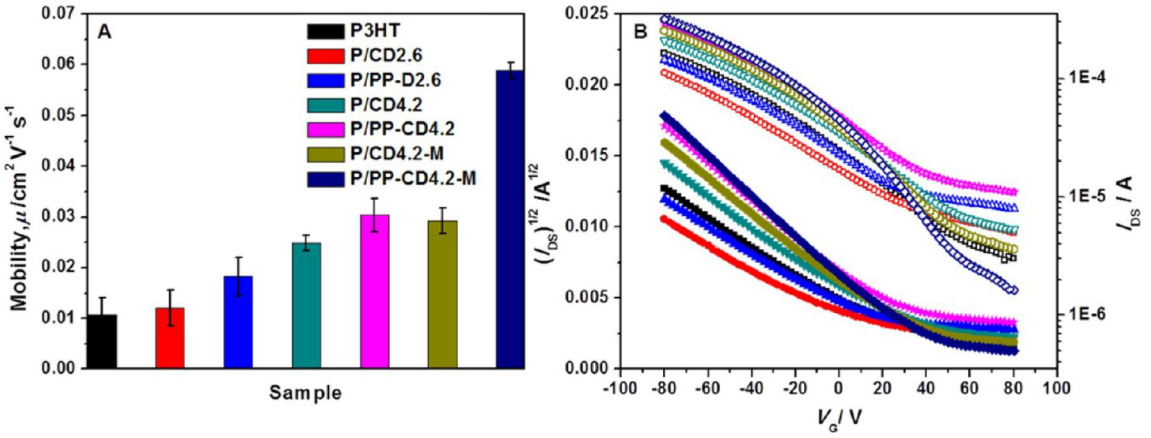

Figure 8. (A) Average field-effect mobility values and (B) associated transfer and output curves for drop-cast films processed from dispersions containing low and high axial ratio particles and pristine P3HT.

3.85 Å in P/CD4.2-M control (Figure S8C) and significantly decreased at 3.67 Å in P/PP-CD4.2-M (Figure 7C), pointing to a more tightly packed crystal structure. Intense in-plane reflections indexed to (100) and centered in the 16.11−16.50 Å *d*-spacing range indicated that the P3HT films consisted of multistacked layers arranged perpendicular to the silicon substrate (Table 3).

Crystal size evaluated from the Scherrer equation revealed significant differences between films processed from low and high axial ratio particles. The data also suggest that the presence of a PSLG shell impacted P3HT packing and crystalline domain size. Irrespective of the particle axial ratio, the 100 peak was significantly narrower in films originated from polypeptide-coated silica dispersions than those containing plain silica domes and pristine P3HT. Crystal size increased with the narrowness of the 100 reflection peak. This trend was more prominent for low axial ratio particles, 94 ± 4 nm (P/PP-CD2.6) versus 81 ± 1 nm (P/CD2.6) and 75 ± 2 nm (P3HT), than for high axial ratio particles, 78 ± 1 nm (P/PP-CD4.2-M) and 76 ± 3 nm (P/PP-CD4.2) versus 71 ± 2 nm (P/CD4.2-M) and 70 ± 2 nm (P/CD4.2). Interestingly, the domain size of crystals was larger in drop-cast films from short (2.6) versus long (4.2) silica dome dispersions. Altogether, the GIWAXS data point to a close-packed P3HT structure with π-stacked conjugated segments characteristic of highly crystalline aggregates. Films prepared from dispersions containing the PSLG particles appeared to be more crystalline than either the PSLG-free controls or P3HT alone.

3.7. Organic Field-Effect Transistor Device Performance. In order to distinguish between the effects of the two axial ratio particles, the electronic performance of the films was evaluated in an OFET device architecture. Figure 8 depicts characteristic OFET transfer and output curves (p-channel) as well as the calculated charge-carrier mobilities.

Introduction of either low or high axial ratio particles into P3HT solutions had no negative effect on charge-carrier transport of the semiconductor. As seen in Figure 8A, in the presence of high axial ratio particles, drop-cast film mobility increased by a factor of 3 versus low axial ratio homologues. For instance, the average mobility of P/PP-CD4.2-M film, which was exposed to an applied magnetic field, was as high as (6 ± 0.16) × 10^{-2} $cm^2 \cdot V^{-1} \cdot s^{-1}$, versus (1.84 ± 0.38) × 10^{-2} $cm^2 \cdot V^{-1} \cdot s^{-1}$ for P/PP-CD2.6. The values of mobility also represent a factor of 6 and 2 increase when compared to pristine P3HT. These results are somewhat surprising given the presence of large particles in the device channel, which are not expected to favor effective transport; particles would likely lead to additional defects and/or grain boundaries and interfere with charge transport. Mobilities calculated for films fabricated after magnetic separation of the dispersions prior to drop-casting suggest that defects did limit transport in particle-containing films. P/PP-CD4.2 exhibited a macroscopic mobility of (3 ± 0.3) × 10^{-2} $cm^2 \cdot V^{-1} \cdot s^{-1}$, which is almost 2 times less than that of the corresponding film after particle magnetic removal. All samples processed from dispersions containing PSLG particles presented higher charge-transport values than their controls. These results indicate that the presence of PSLG may improve the performance of the semiconductor polymer. Importantly, the on−off ratios for P/PP-CD4.2-M films were higher than those for low axial ratio homologues and controls (Figure 8B).

Overall, in the presence of PSLG, conjugated polymer charge-transport performance was noticeably improved in comparison with pristine P3HT. Combined with AFM findings, the OFET results show that PSLG-coated anisotropic particles can stimulate the nucleation and growth of P3HT into the ordered crystalline structures seen as long and aligned fibrils on the substrate. These results confirm the positive impact associated with hydrophobic interactions between P3HT C6 and PSLG C18, as suggested by PiFM data (Figure 1).

3.8. Quantitative Evaluation of P3HT Fiber Physical Parameters. In order to extract more quantitative information about the demonstrated film properties, the FiberApp software[51] was used to evaluate P3HT fiber persistence length, L_p,[52] and contour length, L (Table 4). Slight differences in L_p were apparently associated with variations in the processing approach (e.g., low vs high axial ratio), but drying effects can also influence an accurate evaluation of L. One feature defined

Table 4. Contour and Persistence Lengths of Semiconducting Drop-Cast Films

sample	L (nm)	L_p (nm)
P3HT	1885 ± 932	8616 ± 100
P/CD2.6	509 ± 156	3975 ± 155
P/PP-CD2.6	1748 ± 932	8663 ± 400
P/CD4.2	430 ± 85	2916 ± 160
P/PP-CD4.2	536 ± 130	3836 ± 644
P/CD4.2-M	685 ± 162	7040 ± 495
P/PP-CD4.2-M	533 ± 160	4182 ± 370

all samples: L_p was, on average, 1 order of magnitude higher than L. This finding suggests that highly rigid structures of ordered P3HT chains were necessary to yield highly crystalline films, as evidenced by GIWAXS.

In solution, free P3HT polymer chains adopt a random coil structure with a semiflexible backbone and $L_p \approx 3$ nm.[53] During self-assembly by $\pi-\pi$ stacking, electron delocalization may occur concomitantly with chain planarization. The planar disposition of 3-hexylthiophene units along and relative to P3HT backbone that can propagate over long distances leads to the formation of more rigid rodlike structures that are favorable for efficient charge-carrier transport. The high L_p values extracted from the AFM images signify high stiffness in the P3HT assemblies. On the other hand, effective organization of P3HT polymer chains via $\pi-\pi$ stacking over long distances is reflected by their conjugation length. Consequently, there is a direct correlation between the calculated stiffness of P3HT fibers and their conjugation length.[53]

The above relationship can be further expanded to P3HT crystal size (Table 3) and charge-carrier mobility values (Figure 8A). Whether PSLG was present or not, films processed from low axial ratio particles had larger crystalline domains and smaller mobility values than their high axial ratio homologues. The same trend was observed for films with PSLG versus those without PSLG, regardless of particle axial ratio. The calculated L_p values of P3HT fibers formed in the presence of PSLG were higher than those without PSLG, except the one that was processed by magnetic withdrawal. In this case, particle removal could cause fibril breakage, but instead, this film showed the lowest $\pi-\pi$ stacking distance (3.67 ± 2 nm, Table 3), indicating a tight packing of P3HT chains. These correlations suggest that particle architecture[35] may also play a role in the demonstrated film properties. Both PP-CD particles (2.6 and 4.2) were designed with approximately similar numbers of initiators that enabled the growth of PSLG chains. It is then reasonable to assume that the high axial ratio particles had a sparser coverage with PSLG helical chains than the low axial ratio ones. This feature could favor P3HT chains to penetrate through the particle shell and interact strongly with C18-bearing PSLG helices. Under these conditions, P3HT could easily adopt an extended conformation where the chains become planar relative to the backbone and have fewer defects (e.g., kinks, twists). Such extended P3HT chains pinned to the PSLG helix through entangled C6–C18 arms likely led to effective nucleation and growth of tightly packed structures, as revealed by GIWAXS (Table 3). Conceivably, this dense packing led to rigid fibrils (Table 4) and high charge-carrier mobility values (Figure 8).

4. CONCLUSIONS

Covalently bound PSLG-coated dome-capped cylindrical silica composite particles induced organization of P3HT. The formation of P3HT fibrils in the dispersion state was supported by both AFM imaging of spin-cast films and PiFM. UV–vis spectroscopic analysis demonstrated that planarization of the P3HT polymer backbone was enhanced in the presence of particles, especially PSLG-coated particles, when compared to a pristine P3HT film. Thus, PSLG-primed particles influenced the organization of the conjugated polymer into ordered, optically anisotropic and rigid structures, a characteristic that was evidenced by POM, polarized micro-Raman spectroscopy, and persistence length calculations. Mechanistically, hydrophobic–hydrophobic interactions between the alkyl moieties of P3HT and PSLG shells enabled effective orientation (planarization) of the conjugated polymer chains, promoting their nucleation and growth into organized structures.

The morphology of the films observed in POM and AFM presented undulating periodical patterns that were shaped by the coffee ring and Marangoni effects. In concert, these two natural effects accelerated the interactions between the PSLG shells and P3HT polymer, leading to enhanced alignment of semiconducting fibers on the substrate. GIWAXS revealed that P3HT ordered structures were highly crystalline. PSLG-assisted self-assembly of P3HT chains leading to crystalline structures enabled up to a 6-fold increase in charge-carrier mobility when compared to pristine P3HT, as measured in an OFET device.

Given the apparently favorable hydrophobic interactions between PLSG and P3HT, the integration of polypeptide-based particles may prove advantageous to the design of advanced organic semiconducting materials with improved electronic performance. Integration of polypeptides into manufacturing is also expected to expand the range of organic electronic applications toward printable and wearable electronics, as well as biomedical sensors. The use of bioderived components for processing of active electronic materials also provides a potential route to greener technology solutions.

■ AUTHOR INFORMATION

Corresponding Authors

*(C.R.) E-mail cornelia.rosu@mse.gatech.edu.

*(E.R.) E-mail elsa.reichmanis@chbe.gatech.edu.

ORCID ●

Cornelia Rosu: 0000-0001-8687-7003

Elsa Reichmanis: 0000-0002-8205-8016

Notes

The authors declare no competing financial interest.

■ ACKNOWLEDGMENTS

This work was supported by Grants DMR-1505105 and BMAT-1609058 from the National Science Foundation (NSF). C.R. appreciates support from the Hightower Family Fund (School of Materials Science and Engineering, Georgia Institute of Technology). E.R. acknowledges support from the Brook Byers Institute for Sustainable Systems. C.R. thanks Professor Paul S. Russo (School of Materials Science and Engineering, Georgia Institute of Technology) and Professor Peter Yunker (School of Physics, Georgia Institute of Technology) for helpful discussions. Dr. Jinxin Fu is acknowledged for help with POM imaging. K.P. thanks Dr. Sung Park and William Morrison (Molecular Vista, Inc.) for help with PiFM measurements. We value access to the Stanford Synchrotron

Radiation Lightsource, SLAC National Accelerator Laboratory facilities (supported by the U.S. Department of Energy, Office of Science, and Office of Basic Energy Sciences under Contract DE-AC02-76SF00515). The help with GIWAXS measurements of Dr. Chi Kin Lo (Professor John Reynolds' group, School of Chemistry and Biochemistry, Georgia Institute of Technology) and Dr. Stefan D. Oosterhaut (Professor Michael Toney's group, SLAC) is deeply appreciated.

■ REFERENCES

(1) Facchetti, A. π-Conjugated Polymers for Organic Electronics and Photovoltaic Cell Applications. *Chem. Mater.* **2011**, *23* (3), 733−758.

(2) Koppe, M.; Brabec, C. J.; Heiml, S.; Schausberger, A.; Duffy, W.; Heeney, M.; McCulloch, I. Influence of Molecular Weight Distribution on the Gelation of P3HT and Its Impact on the Photovoltaic Performance. *Macromolecules* **2009**, *42* (13), 4661−4666.

(3) Martin, T. P.; Wise, A. J.; Busby, E.; Gao, J.; Roehling, J. D.; Ford, M. J.; Larsen, D. S.; Moulé, A. J.; Grey, J. K. Packing Dependent Electronic Coupling in Single Poly(3-hexylthiophene) H- and J-Aggregate Nanofibers. *J. Phys. Chem. B* **2013**, *117* (16), 4478−4487.

(4) Aiyar, A. R.; Hong, J.-I.; Izumi, J.; Choi, D.; Kleinhenz, N.; Reichmanis, E. Ultrasound-Induced Ordering in Poly(3-hexylthiophene): Role of Molecular and Process Parameters on Morphology and Charge Transport. *ACS Appl. Mater. Interfaces* **2013**, *5* (7), 2368−2377.

(5) Chang, M.; Choi, D.; Fu, B.; Reichmanis, E. Solvent Based Hydrogen Bonding: Impact on Poly(3-hexylthiophene) Nanoscale Morphology and Charge Transport Characteristics. *ACS Nano* **2013**, *7* (6), 5402−5413.

(6) Choi, D.; Chang, M.; Reichmanis, E. Controlled Assembly of Poly(3-hexylthiophene): Managing the Disorder to Order Transition on the Nano- through Meso-Scales. *Adv. Funct. Mater.* **2015**, *25* (6), 920−927.

(7) Wang, G.; Persson, N.; Chu, P.-H.; Kleinhenz, N.; Fu, B.; Chang, M.; Deb, N.; Mao, Y.; Wang, H.; Grover, M. A.; Reichmanis, E. Microfluidic Crystal Engineering of pi-Conjugated Polymers. *ACS Nano* **2015**, *9* (8), 8220−8230.

(8) Osaka, I.; Takimiya, K. Backbone Orientation in Semiconducting Polymers. *Polymer* **2015**, *59*, A1−A15.

(9) Beiley, Z. M.; Hoke, E. T.; Noriega, R.; Dacuna, J.; Burkhard, G. F.; Bartelt, J. A.; Salleo, A.; Toney, M. F.; McGehee, M. D. Morphology-Dependent Trap Formation in High Performance Polymer Bulk Heterojunction Solar Cells. *Adv. Energy Mater.* **2011**, *1* (5), 954−962.

(10) Lan, Y.-K.; Yang, C. H.; Yang, H.-C. Theoretical Investigations of Electronic Structure and Charge Transport Properties in Polythiophene-based Organic Field-effect Transistors. *Polym. Int.* **2010**, *59* (1), 16−21.

(11) Wood, D.; Hancox, I.; Jones, T. S.; Wilson, N. R. Quantitative Nanoscale Mapping with Temperature Dependence of the Mechanical and Electrical Properties of Poly(3-hexylthiophene) by Conductive Atomic Force Microscopy. *J. Phys. Chem. C* **2015**, *119* (21), 11459−11467.

(12) Vakhshouri, K.; Smith, B. H.; Chan, E. P.; Wang, C.; Salleo, A.; Wang, C.; Hexemer, A.; Gomez, E. D. Signatures of Intracrystallite and Intercrystallite Limitations of Charge Transport in Polythiophenes. *Macromolecules* **2016**, *49* (19), 7359−7369.

(13) Aiyar, A. R.; Hong, J.-I.; Reichmanis, E. Regioregularity and Intrachain Ordering: Impact on the Nanostructure and Charge Transport in Two-Dimensional Assemblies of Poly(3-hexylthiophene). *Chem. Mater.* **2012**, *24* (15), 2845−2853.

(14) Kleinhenz, N.; Persson, N.; Xue, Z. Z.; Chu, P. H.; Wang, G.; Yuan, Z. B.; McBride, M. A.; Choi, D.; Grover, M. A.; Reichmanis, E. Ordering of Poly(3-hexylthiophene) in Solutions and Films: Effects of Fiber Length and Grain Boundaries on Anisotropy and Mobility. *Chem. Mater.* **2016**, *28* (11), 3905−3913.

(15) Crossland, E. J. W.; Rahimi, K.; Reiter, G.; Steiner, U.; Ludwigs, S. Systematic Control of Nucleation Density in Poly(3-Hexylthiophene) Thin Films. *Adv. Funct. Mater.* **2011**, *21* (3), 518−524.

(16) *P3HT Revisited: From Molecular Scale to Solar Cell Devices*; Ludwigs, S., Ed.; Advances in Polymer Science, Vol. *265*; Springer: Berlin and Heidelberg, Germany, 2014; DOI: 10.1007/978-3-662-45145-8.

(17) Fleischli, F. D.; Ghasdian, N.; Georgiou, T. K.; Stingelin, N. Tailoring the Optical Properties of Poly(3-hexylthiophene) by Emulsion Processing Using Polymeric Macrosurfactants. *J. Mater. Chem. C* **2015**, *3* (9), 2065−2071.

(18) Bielecka, U.; Lutsyk, P.; Janus, K.; Sworakowski, J.; Bartkowiak, W. Effect of Solution Aging on Morphology and Electrical Characteristics of Regioregular P3HT FETs Fabricated by Spin Coating and Spray Coating. *Org. Electron.* **2011**, *12* (11), 1768−1776.

(19) Chang, M.; Lee, J.; Kleinhenz, N.; Fu, B.; Reichmanis, E. Photoinduced Anisotropic Supramolecular Assembly and Enhanced Charge Transport of Poly(3-hexylthiophene) Thin Films. *Adv. Funct. Mater.* **2014**, *24* (28), 4457−4465.

(20) Fu, B.; Wang, C.-Y.; Rose, B. D.; Jiang, Y.; Chang, M.; Chu, P.-H.; Yuan, Z.; Fuentes-Hernandez, C.; Kippelen, B.; Brédas, J.-L.; Collard, D. M.; Reichmanis, E. Molecular Engineering of Non-halogenated Solution-Processable Bithiazole-Based Electron-Transport Polymeric Semiconductors. *Chem. Mater.* **2015**, *27* (8), 2928−2937.

(21) Wang, G.; Persson, N.; Chu, P.-H.; Kleinhenz, N.; Fu, B.; Chang, M.; Deb, N.; Mao, Y.; Wang, H.; Grover, M. A.; Reichmanis, E. Microfluidic Crystal Engineering of π-Conjugated Polymers. *ACS Nano* **2015**, *9* (8), 8220−8230.

(22) Park, M. S.; Aiyar, A.; Park, J. O.; Reichmanis, E.; Srinivasarao, M. Solvent Evaporation Induced Liquid Crystalline Phase in Poly(3-hexylthiophene). *J. Am. Chem. Soc.* **2011**, *133* (19), 7244−7247.

(23) Salammal, S. T.; Mikayelyan, E.; Grigorian, S.; Pietsch, U.; Koenen, N.; Scherf, U.; Kayunkid, N.; Brinkmann, M. Impact of Thermal Annealing on the Semicrystalline Nanomorphology of Spin-Coated Thin Films of Regioregular Poly(3-alkylthiophene)s as Observed by High-Resolution Transmission Electron Microscopy and Grazing Incidence X-ray Diffraction. *Macromolecules* **2012**, *45* (13), 5575−5585.

(24) Joshi, S.; Grigorian, S.; Pietsch, U.; Pingel, P.; Zen, A.; Neher, D.; Scherf, U. Thickness Dependence of the Crystalline Structure and Hole Mobility in Thin Films of Low Molecular Weight Poly(3-hexylthiophene). *Macromolecules* **2008**, *41* (18), 6800−6808.

(25) Skrypnychuk, V.; Wetzelaer, G.-J. A. H.; Gordiichuk, P. I.; Mannsfeld, S. C. B.; Herrmann, A.; Toney, M. F.; Barbero, D. R. Ultrahigh Mobility in an Organic Semiconductor by Vertical Chain Alignment. *Adv. Mater.* **2016**, *28* (12), 2359−2366.

(26) Russo, P. S.; Blum, F. D.; Ipsen, J. D.; Abul-Hajj, Y. J.; Miller, W. G. The surface activity of the phytotoxin cerato-ulmin. *Can. J. Bot.* **1982**, *60* (8), 1414−1422.

(27) Kirby, S. M.; Zhang, X.; Russo, P. S.; Anna, S. L.; Walker, L. M. Formation of a Rigid Hydrophobin Film and Disruption by an Anionic Surfactant at an Air/Water Interface. *Langmuir* **2016**, *32* (22), 5542−5551.

(28) Rosu, C.; Kleinhenz, N.; Choi, D.; Tassone, C. J.; Zhang, X.; Park, J. O.; Srinivasarao, M.; Russo, P. S.; Reichmanis, E. Protein-Assisted Assembly of pi-Conjugated Polymers. *Chem. Mater.* **2016**, *28* (2), 573−582.

(29) Schillinger, E.-K.; Mena-Osteritz, E.; Hentschel, J.; Börner, H. G.; Bäuerle, P. Oligothiophene Versus β-Sheet Peptide: Synthesis and Self-Assembly of an Organic Semiconductor-Peptide Hybrid. *Adv. Mater.* **2009**, *21* (16), 1562−1567.

(30) Ardoña, H. A. M.; Tovar, J. D. Peptide π-Electron Conjugates: Organic Electronics for Biology? *Bioconjugate Chem.* **2015**, *26* (12), 2290−2302.

(31) Rosu, C.; Tassone, C. J.; Chu, P.-H.; Balding, P. L.; Gorman, A.; Hernandez, J. L.; Hawkridge, M.; Roy, A.; Negulescu, I. I.; Russo, P. S.; Reichmanis, E. Polypeptide-Assisted Organization of π-Conjugated Polymers into Responsive, Soft 3D Networks. *Chem. Mater.* **2017**, *29* (12), 5058−5062.

(32) Poche, D. S.; Daly, W. H.; Russo, P. S. Synthesis and Some Solution Properties of Poly(γ-Stearyl-α,L-Glutamate). *Macromolecules* **1995**, *28* (20), 6745−6753.
(33) Schmidtke, S.; Russo, P.; Nakamatsu, J.; Buyuktanir, E.; Turfan, B.; Temyanko, E.; Negulescu, L. Thermoreversible Gelation of Isotropic and Liquid Crystalline Solutions of a "Sticky" Rodlike Polymer. *Macromolecules* **2000**, *33* (12), 4427−4432.
(34) Rosu, C.; Balamurugan, S.; Cueto, R.; Roy, A.; Russo, P. S. Polypeptide-Coated Silica Particles Dispersed in Lyotropic Liquid Crystals of the Same Polypeptide. *J. Phys. Chem. B* **2016**, *120* (29), 7275−7288.
(35) Rosu, C.; Jacobeen, S.; Park, K.; Reichmanis, E.; Yunker, P.; Russo, P. S. Domed Silica Microcylinders Coated with Oleophilic Polypeptides and Their Behavior in Lyotropic Cholesteric Liquid Crystals of the Same Polypeptide. *Langmuir* **2016**, *32* (49), 13137−13148.
(36) Clark, J.; Silva, C.; Friend, R. H.; Spano, F. C. Role of Intermolecular Coupling in the Photophysics of Disordered Organic Semiconductors: Aggregate Emission in Regioregular Polythiophene. *Phys. Rev. Lett.* **2007**, *98* (20), No. 206406.
(37) Kleinhenz, N.; Rosu, C.; Chatterjee, S.; Chang, M.; Nayani, K.; Xue, Z.; Kim, E.; Middlebrooks, J.; Russo, P. S.; Park, J. O.; Srinivasarao, M.; Reichmanis, E. Liquid Crystalline Poly(3-hexylthiophene) Solutions Revisited: Role of Time-Dependent Self-Assembly. *Chem. Mater.* **2015**, *27* (7), 2687−2694.
(38) Niles, E. T.; Roehling, J. D.; Yamagata, H.; Wise, A. J.; Spano, F. C.; Moule, A. J.; Grey, J. K. J-Aggregate Behavior in Poly-3-hexylthiophene Nanofibers. *J. Phys. Chem. Lett.* **2012**, *3* (2), 259−263.
(39) Belfiore, L. A. Basic Concepts and Molecular Optical Anisotropy in Semicrystalline Polymers. In *Physical Properties of Macromolecules*; John Wiley & Sons, Inc.: 2010; pp 247−286; DOI: 10.1002/9780470551592.ch7.
(40) Kozawaguchi, H.; Wada, M. Helical Twisting Power in Cholesteric Liquid Crystal Mixtures. I. Experimental Results. *Jpn. J. Appl. Phys.* **1975**, *14* (5), 651.
(41) Nakagiri, T. Helical Twisting Power in Mixtures of Nematic and Cholesteric Liquid Crystals. *Phys. Lett. A* **1971**, *36* (5), 427−428.
(42) Wensink, H. H.; Jackson, G. Generalized Van der Waals Theory for the Twist Elastic Modulus and Helical Pitch of Cholesterics. *J. Chem. Phys.* **2009**, *130* (23), No. 234911.
(43) Deegan, R. D.; Bakajin, O.; Dupont, T. F.; Huber, G.; Nagel, S. R.; Witten, T. A. Contact Line Deposits in an Evaporating Drop. *Phys. Rev. E: Stat. Phys., Plasmas, Fluids, Relat. Interdiscip. Top.* **2000**, *62* (1), 756−765.
(44) Deegan, R. D.; Bakajin, O.; Dupont, T. F.; Huber, G.; Nagel, S. R.; Witten, T. A. Capillary Flow as the Cause of Ring Stains from Dried Liquid Drops. *Nature* **1997**, *389* (6653), 827−829.
(45) Dupeyrat, M.; Nakache, E. 205 - Direct Conversion of Chemical Energy Into Mechanical Energy at an Oil Water Interface. *Bioelectrochem. Bioenerg.* **1978**, *5* (1), 134−141.
(46) Scriven, L. E.; Sternling, C. V. The Marangoni Effects. *Nature* **1960**, *187* (4733), 186−188.
(47) Yunker, P. J.; Still, T.; Lohr, M. A.; Yodh, A. G. Suppression of the Coffee-ring Effect by Shape-dependent Capillary Interactions. *Nature* **2011**, *476* (7360), 308−311.
(48) De Dier, R.; Sempels, W.; Hofkens, J.; Vermant, J. Thermocapillary Fingering in Surfactant-Laden Water Droplets. *Langmuir* **2014**, *30* (44), 13338−13344.
(49) Weon, B. M.; Je, J. H. Fingering Inside the Coffee Ring. *Phys. Rev. E* **2013**, *87* (1), No. 013003.
(50) Still, T.; Yunker, P. J.; Yodh, A. G. Surfactant-Induced Marangoni Eddies Alter the Coffee-Rings of Evaporating Colloidal Drops. *Langmuir* **2012**, *28* (11), 4984−4988.
(51) Usov, I.; Mezzenga, R. FiberApp: An Open-Source Software for Tracking and Analyzing Polymers, Filaments, Biomacromolecules, and Fibrous Objects. *Macromolecules* **2015**, *48* (5), 1269−1280.
(52) Wang, H. H.; Dupre, D. B. Orientational Order in Liquid-crystal Solutions Polyhexylisocyanate 0.1. Infrared Dichroism. *J. Chem. Phys.* **1992**, *96* (2), 1523−1529.
(53) McCulloch, B.; Ho, V.; Hoarfrost, M.; Stanley, C.; Do, C.; Heller, W. T.; Segalman, R. A. Polymer Chain Shape of Poly(3-alkylthiophenes) in Solution Using Small-Angle Neutron Scattering. *Macromolecules* **2013**, *46* (5), 1899−1907.